Functional Composite Materials

RESEARCH

Open Access

Electromagnetic interference shielding properties of PMMA modified-$Co_{0.5}Zn_{0.5}Fe_2O_4$ – polyaniline composites

Parthasarathi Bera[1*], R. V. Lakshmi[1*], R. P. S. Chakradhar[1], Suryasarathi Bose[2] and Harish C. Barshilia[1]

Abstract

Present work reports solution combustion synthesis (SCS) of $Co_{0.5}Zn_{0.5}Fe_2O_4$ spinel ferrite, its chemical modification with polymethylmethacrylate (PMMA), synthesis of polyaniline (PANI), and electromagnetic interference (EMI) shielding properties of their composites. Both as-prepared and PMMA-modified $Co_{0.5}Zn_{0.5}Fe_2O_4$ adopt cubic spinel structure as shown by X-ray diffraction studies. Field emission scanning electron microscopy images show the agglomerated and microporous nature of the ferrites. High resolution transmission electron microscopy image of as-prepared $Co_{0.5}Zn_{0.5}Fe_2O_4$ shows lattice fringes related to (311) plane of the spinel structure. X-ray photoelectron spectroscopy studies reveal the presence of Co^{2+}, Zn^{2+}, and Fe^{3+} in tetrahedral and octahedral coordinations in the ferrite. EMI shielding properties are evaluated for PMMA-modified $Co_{0.5}Zn_{0.5}Fe_2O_4$ and PANI composites in different weight ratios. Composites containing PMMA-modified ferrite and PANI with 50:50 and 10:90 weight ratios show the best performance among all the composites in 2–20 GHz frequency range. Optimized PMMA-modified $Co_{0.5}Zn_{0.5}Fe_2O_4$ and PANI composite with the ratio of 10:90 shows shielding effectiveness (SE) values of −16.6 to −24.2 dB in 2–20 GHz frequency region.

Keywords EMI shielding, $Co_{0.5}Zn_{0.5}Fe_2O_4$, Solution combustion synthesis, PMMA modification, Polyaniline

*Correspondence:
Parthasarathi Bera
partho@nal.res.in
R. V. Lakshmi
lakshmi_rv@nal.res.in
Full list of author information is available at the end of the article

Graphical Abstract

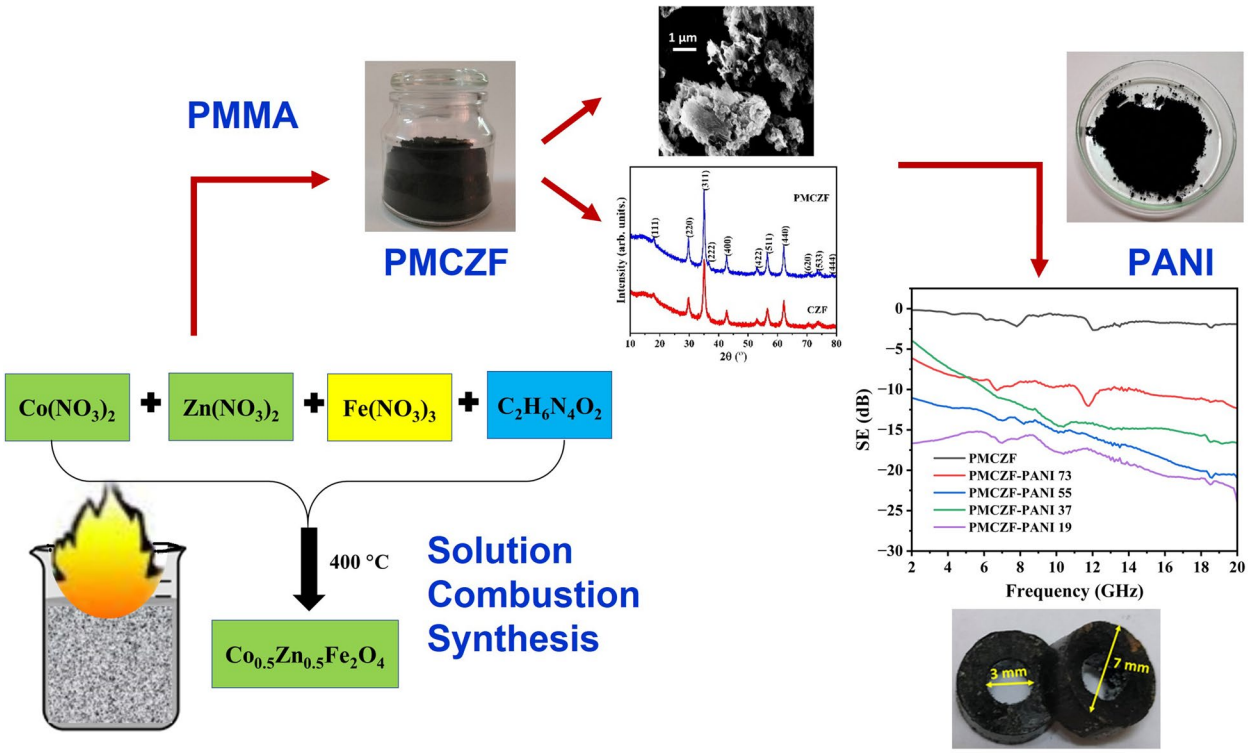

Introduction

In last several years, world has been witnessing very rapid growth of electronic and communication systems in terms of massive development of advanced electronic science, technology, and products. The recent advancement of electrical and electronic devices and systems such as televisions, radios, computers, mobile phones, gadgets, local area networks, and satellite broadcast systems, etc. has made human life easier, comfortable, and luxurious. In this sense, it is to be noted that electromagnetic (EM) radiation is used by high-frequency electrical systems and telecommunication devices to send data across long distances. The use of electronic devices has been increased in automated industries, homes, workplaces, medical facilities, airports, military installations, automobiles, aircrafts, and satellites. At the same time, the widespread use of smart electronic control and communication devices in such areas creates electromagnetic interference (EMI) which has become a serious concern in the modern society [1–3]. It has been observed that use of electronic equipment and wireless devices disrupts the surrounding environment and emits EM radiation. Particularly, EMI is defined as a reduction in the performance of a device or a system caused by unforeseen conductance or radiance of signals from other electronic or electrical devices. Moreover, EMI can damage DNA strands, weaken biological immune systems, stimulate cancer, and overall pose a threat to human health [4, 5]. EM radiation is also produced by the natural occurrences including solar flare, thunder, and electrostatic discharge. Due to interference with sensitive electronic equipment such as radars, antenna systems, and military electronic control systems, etc. these waves produce noise. Various agencies including defence, national security, banking, etc. experience security threat as a result of EM wave interference with data center servers and networking equipment. In this aspect, using shielding materials to protect electronic devices and circuits from EMI has become crucial. Consequently, materials for EMI shielding by means of EM wave reflecting or absorbing have gained global attention and are widely used in civil, commercial, and military applications. By absorbing EM wave and transforming it into thermal and other forms of energy, EM wave absorbers efficiently increase EMI shielding, thereby minimizing EM radiation. The efficiency and lifespan of electrical and electronic devices are increased by EMI shielding, which also lowers the likelihood that these issues may arise. These materials

have been used as sheets, paints, coatings, inks, ceramic tiles, textile fabrics, and powders loaded into matrix composites or combinations with conducting materials.

Two primary processes in the EMI shielding mechanism are reflection and absorption of EM radiation. It is preferable to shield electronic gadgets through absorption rather than reflection. This is so that the surrounding environment may be impacted by reflected radiation. Reflection mechanism considers the impedance mismatch of material with the surrounding medium which causes radiation to bounce off from it. Conductive materials exhibit a significant impedance mismatch. Materials with both electric and magnetic characteristics can enhance shielding through absorption. The shielding efficiency (SE) of a typical EMI shielding material is associated with reflection (SE_R), absorption (SE_A), and multiple internal reflections (SE_{MR}) [6, 7]. SE_R is usually considered to be the result of an impedance mismatch between the free space and shielding materials. Sum of the effects of dielectric and magnetic loss is SE_A. An important condition for the absorption of EM wave is degree of matching between dielectric loss and magnetic loss. Hence, according to EMI shielding principles, shielding materials are of two types: (a) EM wave-reflecting materials and (b) EM wave-absorbing materials. EM wave-reflecting materials contain abundant mobile charge carriers which interact with electric vector of incident EM wave. Further, EM wave is made up of both electric and magnetic fields which are perpendicular to each other. It is needed to cancel or nullify both of these components for absorbing the EM wave. In this regard, EM wave-absorbing materials consisting of electric and/or magnetic dipoles interact with electric (E) and magnetic vectors (H) of the incident EM wave so that these component vectors are necessarily to be nullified for effective absorption of EM wave. EMI shielding effectiveness by absorption mechanism depends on electrical conductivity and relative permeability of the material which indicates that a good EM wave-absorbing material should possess high electrical conductivity and high permeability. Hence, EM wave-absorbing materials are the combination of dielectric materials and magnetic materials. Dielectric loss materials mostly lose EM waves due to polarization of the electrons, molecules, or interfacial polarization of the medium [8] and magnetic loss materials lose EM wave through magnetic interaction. However, it is difficult for a single material to provide expected EMI shielding property. In this regard, composite materials with a combination of two or three components may show excellent EMI shielding property having improved impedance match between dielectric and magnetic losses and also a synergistic effect between EM wave absorption and reflection.

Due to their high electrical conductivity and dielectric permittivity, metals are most often used materials for EMI shielding, wherein mechanism is of EM wave reflection type [7]. However, metals have drawbacks such as their weight, susceptibility to corrosion, lack of flexibility, and difficult processing. In recent days, as electronic devices are compact, researchers across the world have put more effort to develop new generation excellent EMI shielding materials, which contain unique characteristics such as low cost, easy to synthesize, light weight, thin, improved corrosion resistance, mechanical flexibility, etc. In order to overcome the limitations of metal-based EMI shielding materials, huge attention has been paid for the development of polymer-based composite materials because of their easy processability, high flexibility, low density, excellent chemical and corrosion resistance, and tunable structural and mechanical properties. As a result, in the recent decades, a variety of materials and their composites have been investigated for use in EMI shielding applications. These materials include very thin sheets of metals, various carbon materials such as graphite, graphene, reduced graphene oxide, carbon black, carbon fibers, single or multiwalled carbon nanotubes (CNTs), and conductive polymers, dielectric and semiconducting materials such as $BaTiO_3$, ZnO, and SiC, and magnetic materials such as spinel ferrites and hexaferrites [9–21]. It is also to be mentioned that different new generation emerging materials such as sulfides, phosphides, nitrides, metal organic frameworks (MOF), polymer composites, MXenes, carbon hollow microspheres, glass microspheres, ferrite hollow microspheres and nanospheres, etc. have been investigated for EM wave absorbing application [9, 10, 12, 22–34].

In last several years, composites containing ferrites and electrically conducting polymers have been used for EMI shielding application [13, 14, 35]. Among all conducting polymers, polyaniline (PANI) is the most promising for various prospective applications due to its low density, easy manufacture, tunable electrical conductivity, outstanding environment stability, and affordability. As per literature, $CoFe_2O_4$-based composites demonstrate very good EM wave absorbing property. Gulzar et al. have shown total shielding effectiveness value of 35 dB in $CoFe_2O_4$, fly ash, and polyurethane composites in 0.1−20 GHz frequency region [36]. Ahmad et al. have demonstrated the suitability of $CoCe_{0.05}Fe_{1.95}O_4$-polypyrrole composite for EMI shielding application for X-band (8−12 GHz) frequency [37]. In a work of Chahar et al., total shielding effectiveness value of 25.8–27.2 dB is observed for $Co_{0.5}Zn_{0.5}FeO_4$ in the 8.4−12.4 GHz frequency region [38]. However, value has been increased when MWCNTs are mixed with $Co_{0.5}Zn_{0.5}FeO_4$. Sun and coworkers

have investigated microwave absorbing properties of copper-cobalt-nickel ferrite/graphene oxide/polyaniline composites in 2–18 GHz frequency region [39]. Kuekha et al. have demonstrated EMI shielding properties of Ni^{2+}-substituted $CoFe_2O_4$ and polyvinyl alcohol composites [40]. Optimized composite shows total shielding effectiveness value of 27 dB in the X-band frequency region. Recently, our group has prepared $MnFe_2O_4$ by SCS method and then modified with polymethyl methacrylate (PMMA) [41]. Oxidative chemical polymerization method with ammonium peroxodisulfate has been used to prepare PANI. Optimized composite consisting of chemically modified $MnFe_2O_4$ and PANI show total shielding effectiveness value of 44 dB in the X band region (8–12 GHz). According to present literature, in several instances, preparation routese are very involved processes and EMI property has been investigated for X-band frequency only. Studies on EMI shielding properties of Zn^{2+}-substituted $CoFe_2O_4$ and PANI composites are limited in the literature. Recently, our group has reported preparation, characterization, and magnetic properties of $Co_{0.5}Zn_{0.5}FeO_4$ spinel ferrite [42]. In this aspect, the present work reports the modification of SCS-made $Co_{0.5}Zn_{0.5}FeO_4$ by PMMA and preparation of PMMA-modified $Co_{0.5}Zn_{0.5}FeO_4$–PANI composites. EMI shielding properties of these composites have been explored in 2–20 GHz frequency region. For an optimized composition of the $Co_{0.5}Zn_{0.5}FeO_4$–PANI nanocomposite with 10:90 weight ratio shows total shielding efficiency value > 20 dB in higher frequency region of 13–20 GHz indicating that composition can be useful for higher frequency EMI shielding application.

Experimental details

Materials

Precursors for the preparation of $Co_{0.5}Zn_{0.5}Fe_2O_4$ by SCS route were cobalt nitrate ($Co(NO_3)_2$), zinc nitrate ($Zn(NO_3)_2$), and ferric nitrate ($Fe(NO_3)_3$) and were purchased from Loba Chemie. Oxalyl dihydrazide ($C_2H_6N_4O_2$, ODH) was used as fuel for SCS method of preparation of $Co_{0.5}Zn_{0.5}Fe_2O_4$ and was synthesized in the laboratory. Diethyl oxalate and hydrazine hydrate, procured from Loba Chemie, were used for the preparation of ODH. PMMA and N, N dimethyl formamide (DMF) used for the modification of $Co_{0.5}Zn_{0.5}Fe_2O_4$ were obtained from Alfa Aesar and Merck, respectively. Aniline and ammonium peroxodisulfate (APS) were obtained from Loba Chemie, whereas ethanol, isopropyl alcohol, and HCl were obtained from Merck for the synthesis of PANI. All chemicals were used as-supplied. When necessary, Milli-Q water was utilized to prepare solutions.

Preparation of ODH

ODH is commonly used as a fuel for preparation of oxides by SCS synthesis method. It is usually synthesized in the laboratory by a simple precipitation method at a very low temperature. Reactants for the preparation of ODH are diethyl oxalate and hydrazine hydrate. In a typical preparation, 210 mL of diethyl oxalate was taken in a 1000 mL beaker and 150 mL of hydrazine hydrate was added drop by drop into the diethyl oxalate taken in a reaction vessel using a burette. A chiller was used to keep the reaction temperature at less than 5 °C, and the mixture was constantly stirred. A thick white precipitate was formed. It was washed thoroughly with water followed by ethanol and dried at ambient temperature.

Preparation of $Co_{0.5}Zn_{0.5}Fe_2O_4$ by SCS method

$Co_{0.5}Zn_{0.5}Fe_2O_4$ was synthesized by SCS method using $Co(NO_3)_2$, $Zn(NO_3)_2$, and $Fe(NO_3)_3$ as precursors of Co, Zn, and Fe and ODH was used as the fuel. Required amounts for the combustion reaction to prepare $Co_{0.5}Zn_{0.5}Fe_2O_4$ were calculated according to the literature [43]. In a typical preparation, 2 g $Co(NO_3)_2$, 2.04 g $Zn(NO_3)_2$, 11.1 g of $Fe(NO_3)_3$, and 6.5 g ODH were dissolved in water in a 300 mL glass dish. The dish was kept in a furnace preheated at 400 °C. In the initial stage, the solution boiled with frothing, foaming, and experienced dehydration. The combustion started with a burning flame on the surface at the point of complete dehydration, which resulted in a blackish brown voluminous solid product within 5 min. After allowing the product to reach room temperature, it was ground with a mortar and pestle, and was kept inside an airtight bottle. The obtained $Co_{0.5}Zn_{0.5}Fe_2O_4$ is designated as CZF.

Modification of $Co_{0.5}Zn_{0.5}Fe_2O_4$ with PMMA

SCS-derived $Co_{0.5}Zn_{0.5}Fe_2O_4$ and PMMA were taken in the weight ratio (%) of 60:40 and mixed thoroughly in an agate mortar for 15 min. The composite mixture was dispersed in 40–50 mL of DMF using a magnetic stirrer in a reagent bottle for overnight and then ultra-sonicated for 30 min. A brownish precipitation formed when the mixture was transferred into a beaker with 100 mL of Milli-Q water and stirred. Using Whatman 42 filter paper, the precipitate was collected, dried at room temperature, and then placed in an air oven set to 70 °C for the entire night. The dried $Co_{0.5}Zn_{0.5}Fe_2O_4$–PMMA was grounded into powder using an agate mortar for further usage and it is designated as PMCZF.

Preparation of polyaniline

Due to its adjustable electrical conductivity, which can change from an entirely non-conductive substance (insulator) to a metal-like behavior, PANI is a significant

conductive polymer that is frequently utilized. HCl has been a common doping acid or counter ion used in the synthesis which is reported to provide very good electrical conductivity. HCl-doped PANI was synthesized as per the procedure given in the literature [44]. In a typical preparation, 40 mL of aniline was taken in a 1000 mL beaker and 500 mL of 1N HCl was added with stirring for 45 min at 0–2 °C. Aniline hydrochloride was formed when the solution turned colorless. Next, using a burette and constant stirring, 250 mL of a 1 M APS solution (57 g) was gradually added to the mixture dropwise. Temperature was kept constant at < 3 °C to get better conductivity of the polyaniline. The colorless liquid started to turn green which gradually darkened. The solution was left overnight in the same container with stirring. Using vacuum suction with a Whatman 42 filter paper the obtained precipitate was filtered and was thoroughly washed with about 250 mL of 1 N HCl for 3–4 times. Finally, it was washed with isopropyl alcohol till the washing became colorless, confirming that all oligomers were removed. The product finally was a dark greenish powder which was stored in an airtight container. Conductivity of obtained polyaniline was around 1 S cm^{-1}.

Preparation of PMCZF – PANI composites

To prepare PMCZF–PANI composites, they were mixed with various weight ratios. The amounts of PMCZF were taken in 10, 30, 50, and 70 wt.% and the remaining amount was PANI. For uniform mixing the mixtures were blended well in a mortar and pestle. The composite named PMCZF–PANI 19 contains 10 wt.% PMCZF and 90 wt.% PANI. Likewise, PMCZF–PANI 37, PMCZF–PANI 55, and PMCZF–PANI 73 are the designations for the 30–70 wt.%, 50–50 wt.%, and 70–30 wt.% composites, respectively.

Characterization

Structure of as-prepared CZF and PMCZF were analysed with an X-ray powder diffractometer (XRD) from Bruker (Model D8 Advance) operated with CuKα radiation (λ = 1.5406 Å) at 35 kV and 10 mA. The XRD data of the samples were recorded over 2θ range of 10–80° with a scan rate of 0.02 s per step.

Field emission scanning electron microscopy (FESEM) from Carl Zeiss (Supra VP40) equipped with an energy dispersive X-ray spectrometer (EDXS) from Oxford Instruments was utilized to assess the morphologies of as-prepared CZF and PMCZF nanoferrite particles. To obtain FESEM images, as-prepared CZF and PMCZF were dispersed in ethanol and drop-casted on polished metallic substrate from a micropipette. The FESEM instrument had a resolution of 1.2 nm at 10 kV, while the EDXS had a resolution of 133 eV at 5.9 kV.

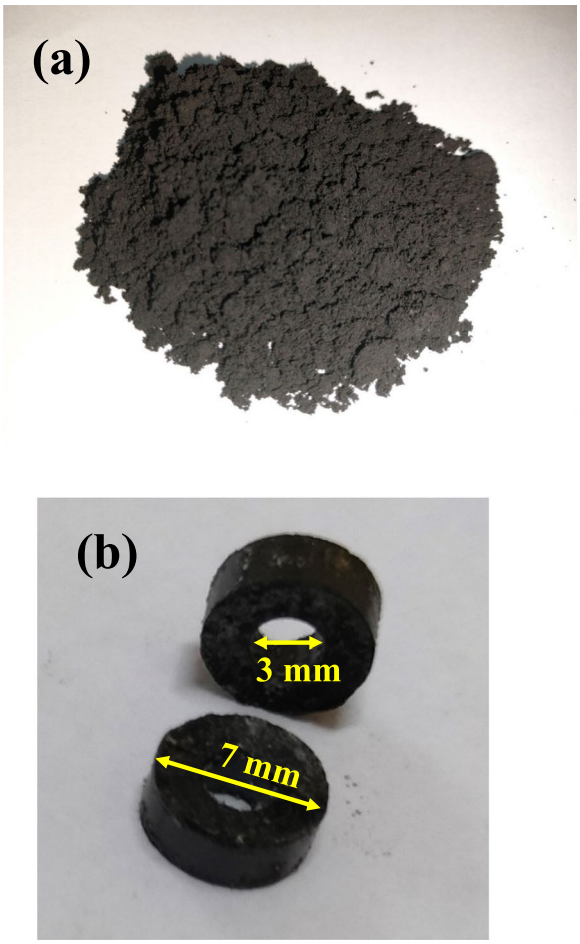

Fig. 1 Typical images of PMCZF–PANI 73 composite: (**a**) powder sample and (**b**) toroidal samples

Analysis of microstructure of CZF nanoferrite particles was carried out by transmission electron microscopy (TEM) and high-resolution transmission electron microscopy (HRTEM) using Tecnai G-20 operated at 200 kV. Same instrument was used for selected area electron diffraction (SAED) and EDXS data. An eppendorf was used to have a minimum of 1 mg of solid ferrite sample. After dispersing the material in 1 mL of ethanol, the mixture was sonicated for a minimum of 15 min. The sample solution was drop-casted on a carbon-coated copper grid kept on a petri dish, then the sample was placed in a vacuum-desiccator.

X-ray photoelectron spectroscopy (XPS) data of as-prepared CZF were collected with a SPECS spectrometer (Germany) using non-monochromatic MgKα radiation (1253.6 eV) as an X-ray source run at 150 W (12 kV, 12.5 mA). Non-monochromatic MgKα radiation (1253.6 eV) was used for recording XPS data of CZF as Co and Fe Auger peaks and 2p core level peaks overlap with each other. The C 1s peak at 284.6 eV used as

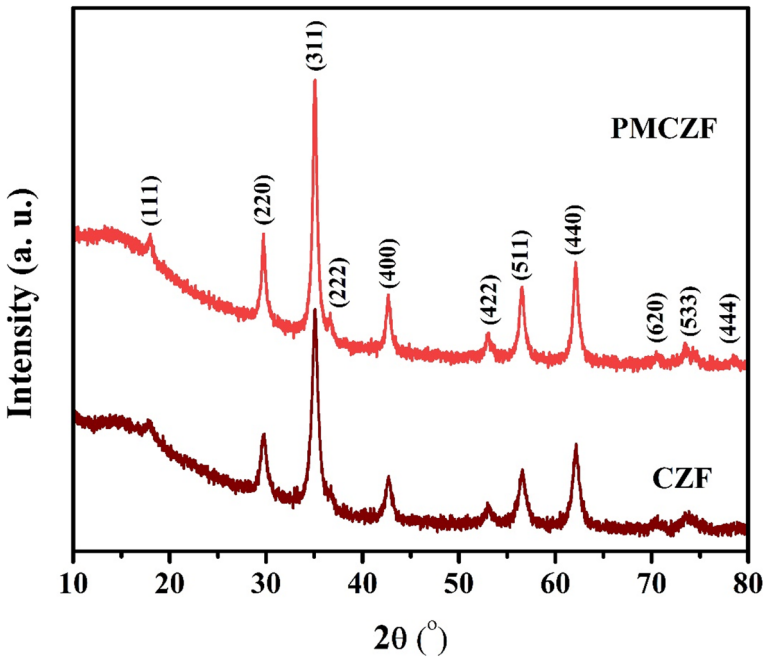

Fig. 2 XRD patterns of CZF and PMCZF

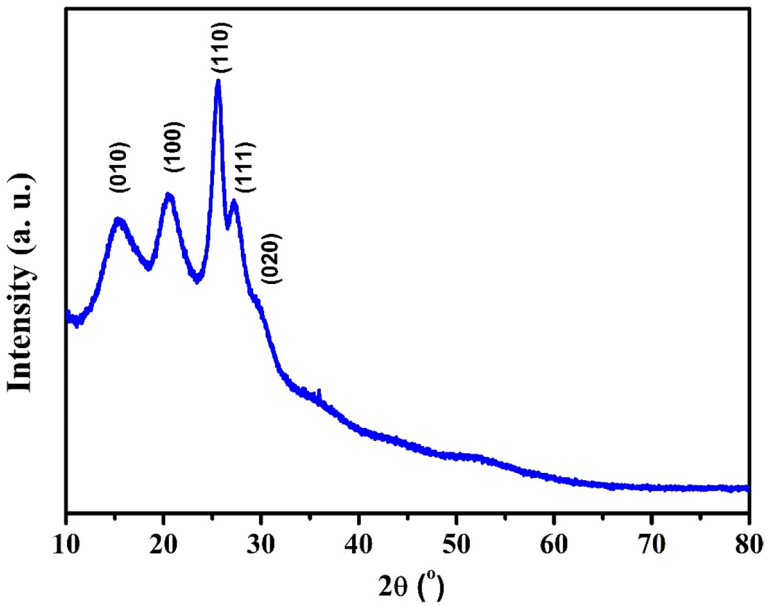

Fig. 3 XRD pattern of PANI

a reference for the binding energies presented here. A pass energy and step increment of 40 and 0.05 eV were used to record all individual core level spectra. For XPS analysis, CZF powder was made into a pellet of 10 mm diameter with 0.5 mm thickness, mounted on the sample holder, and was kept into a load-lock chamber with an ultrahigh vacuum (UHV) of 8×10^{-8} mbar for 5 h for desorbing any volatile species present on the surface. After 5 h in vacuum, the sample was moved into the analysing chamber with UHV of 5×10^{-9} mbar, and XPS data were recorded. To evaluate different component species of Co, Zn, and Fe present in CZF, curve-fitting of their individual core level spectra were carried out using CasaXPS software.

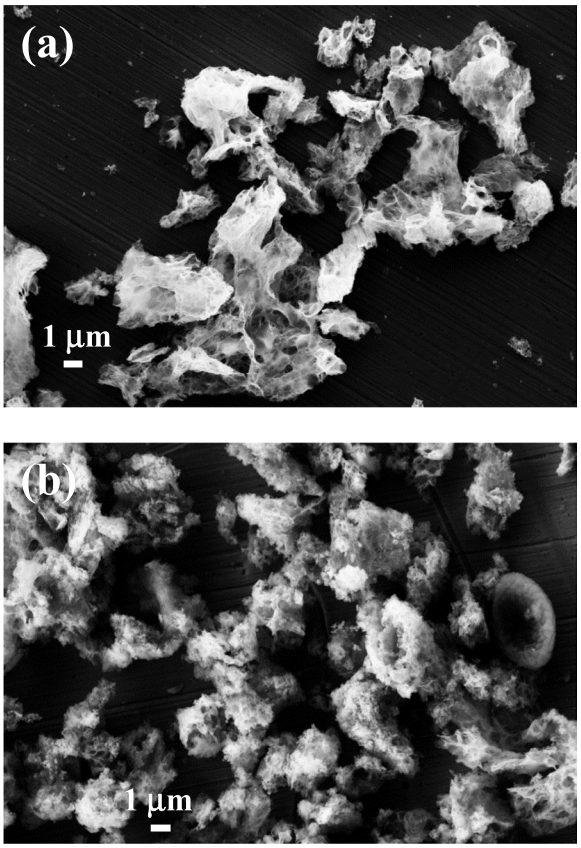

Fig. 4 FESEM images of (**a**) CZF and (b) PMCZF powders

PerkinElmer, Model Frontier IR spectrometer with 4 cm^{-1} resolution was employed to record FTIR spectra of CZF and PMCZF. Attenuated total reflection (ATR) accessory was used to get the spectra.

DILOR-JOBIN–YVON SPEX made LABRAM 010A with He–Ne laser source was employed to record Raman spectra of CZF and PMMA-modified CZF. The wavelength of source was 632.8 nm with a resolution of 4 cm^{-1}.

The magnetic characteristics of PMCZF–PANI composites were evaluated using a vibrating sample magnetometer (VSM) instrument from Lakeshore (Model 7400 series) up to a field range of 1.5 T with a 1.2 inch gap between the pole caps. The pellets of PMCZF–PANI composites with size less than 5 mm × 5 mm were weighed and mounted in the sample holder.

EMI shielding characteristics of PMCZF–PANI composites were studied in coaxial mode employing Anritsu MS4642A vector network analyzer (VNA) coupled with coax (Damaskos M07T) set up. Toroidal samples of 7 mm outer diameter and 3 mm inner diameter with ~ 2 mm thicknesses were made from the composites using a stainless steel die and their different scattering (S) parameters were measured. Typical images of final developed composite material (PMCZF–PANI 73) and its toroidal samples for VNA measurements are shown in Fig. 1.

Results and discussion

XRD studies

Figure 2 displays XRD patterns of CZF and PMCZF. The diffraction peaks are found to be broad indicating the nanocrystalline nature of the ferrites. The diffraction peaks at $2\theta = 17.9°$, 29.7°, 35.2°, 36.6°, 42.7°, 52.9°, 56.7°, 62.1°, 70.7°, 73.5°, and 78.6° correspond to (111), (220), (311), (222), (400), (422), (511), (440), (620), (533), and (444) reflection planes, which are associated with cubic lattice of spinel ferrites agreeing with JCPDS No. 22–1086. Co, Zn, and Fe oxides impurities are not seen in the diffraction patterns. XRD patterns of CZF and PMCZF look to be similar.

The crystallite sizes of CZF and PMCZF ferrites have been estimated from the diffraction patterns using the

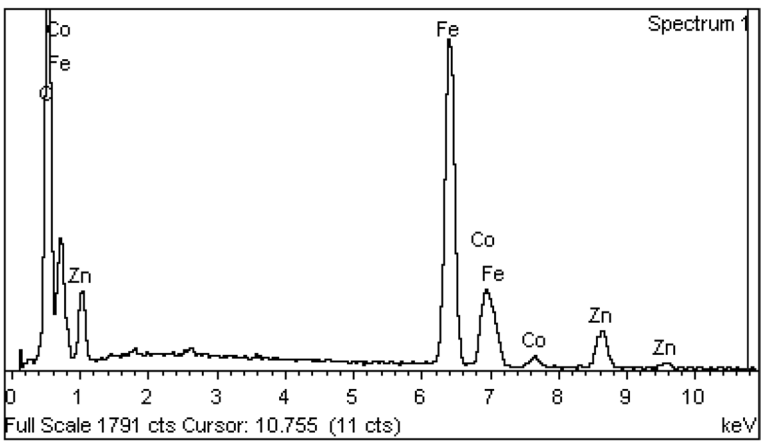

Fig. 5 EDXS data of CZF powder

Table 1 Chemical compositions of CZF evaluated from EDXS studies

Element	Weight %	Atomic %
Co K	12	6.5
Zn K	12.7	6.2
Fe K	44.1	25.2
O K	31.2	62.1

Scherrer's equation considering intense (311) peak as given below:

$$D = \frac{0.94\lambda}{\beta cos\theta} \quad (1)$$

where D is crystallite size, λ is X-ray wavelength in nm, β is full-width-at-half-maximum (FWHM) of the diffraction peak in radian, and θ is Bragg angle. The crystallite sizes of CZF and PMCZF are found to be 13.1 and 16.5 nm, respectively. From their XRD patterns, the lattice parameters are evaluated using the following equation:

$$a = d_{hkl}\sqrt{h^2 + l^2 + k^2} \quad (2)$$

where a is lattice parameter, d_{hkl} is inter planar spacing, and (hkl) is Miller indices. Lattice parameters are found to be 8.4763 Å and 8.4962 Å for CZF and PMCZF, respectively.

Figure 3 represents the powder XRD pattern of HCl-doped PANI. It is a heterogeneous system having moderately crystalline region dispersed in an amorphous phase. Because of the parallel and perpendicular periodicity of the polymer chain broad, diffraction peaks are found between 10 to 30°. Diffraction peaks at 2θ = 15.3°, 20.6°, 25.6°, 27.2°, and 29.3° are indicative the orthorhombic structure of emeraldine salt. The peaks correspond to the (010), (100), (110), (111), and (020) planes of PANI, respectively. XRD pattern of PANI agrees with the pattern available in the literature [45].

FESEM and EDXS studies

Micrographic images of the CZF and PMCZF are displayed in Fig. 4. There looks to be a significant amount of particle agglomeration. Strong magnetic dipole interactions and high surface activity are the primary causes for this agglomeration, which makes them difficult to disperse uniformly. In as-prepared CZF, presence of large voids is observed in its image revealing its highly porous nature. They do not show any well-defined shape. The average particle sizes are in the range of 500 nm to 2 μm. Image of PMCZF is also shown in the figure to compare with CZF. There may be a polymeric layer on the ferrite surface as observed in the FESEM image which is due to the modification of CZF with PMMA.

EDXS analysis of CZF as shown in Fig. 5 reveals the presence of Co, Zn, Fe, and O in CZF. Concentrations of Co, Zn, Fe, and O are found to be 6.5, 6.2, 25.2, and 62.1 at.%, respectively, which is summarized in Table 1. Chemical composition evaluated from EDXS analyses demonstrate that elemental concentrations in CZF are in stoichiometric quantities.

TEM studies

TEM studies have been carried out to assess morphology, particle size, and microstructure of as-prepared $Co_{0.5}Zn_{0.5}Fe_2O_4$. Figure 6a shows a typical bright- field image of CZF. Nanoparticles are homogenously distributed as evident from the image and they are found to be predominately spherical in shape. Sizes pf nanocrystallites estimated from TEM studies are closer to the values calculated from XRD patterns. The HRTEM image of the sample has also been obtained to understand the nanocrystallinity of the sample. Image related to detailed HRTEM analysis of the sample as displayed in Fig. 6b shows highly ordered lattice fringes with a fringe separation of about 2.56 Å, which is associated with (311) lattice plane of the CZF spinel structure. Figure 6c displays selected area electron diffraction (SAED) pattern of the sample. Cubic crystallinity related to spinel structure is clearly evident from the SAED pattern. Thus, microstructural studies confirm the formation of $Co_{0.5}Zn_{0.5}Fe_2O_4$ phase. EDXS of the sample as presented in Fig. 6d also provides evidence of the presence of corresponding elements.

XPS studies

Understanding surface composition and elemental oxidation states in materials can be accomplished employing XPS technique. Notably, it can be used to determine change in metal binding energy caused by variation in the coordination environment with oxygen ions. In the present study, XPS has been used to characterize CZF cubic spinel. A site usually exists in + 2 oxidation state with tetrahedral coordination and B site is in + 3 oxidation state with octahedral coordination in the AB_2O_4 spinel structure. In the case of inverse spinel, A completely occupies octahedral coordination sites while B are in both tetrahedral and octahedral sites. Therefore, binding energies of A and B will vary depending on their coordination sites. Accordingly, Co and Zn will be in + 2 oxidation states with different binding energies and similarly, Fe is to be in + 3 oxidation state with varying binding energies. However, due to the variable oxidation states, there may be some chance of exchange of Co, Zn, and Fe sites in CZF. It is to be noted that studies using XPS can offer

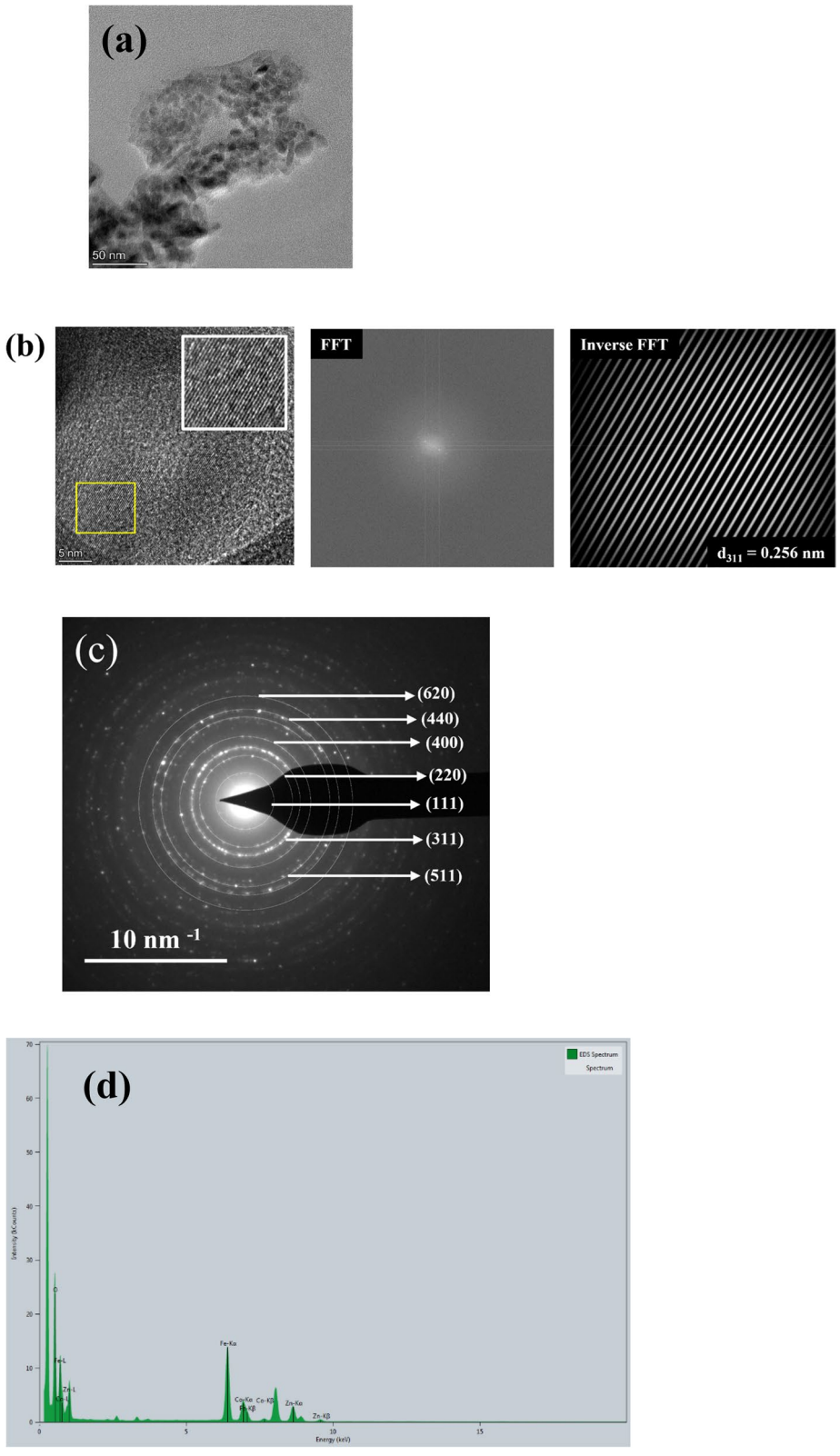

Fig. 6 TEM data of CZF: (**a**) bright-field image, (**b**) detailed HRTEM, (**c**) SAED pattern, and (**d**) EDXS data

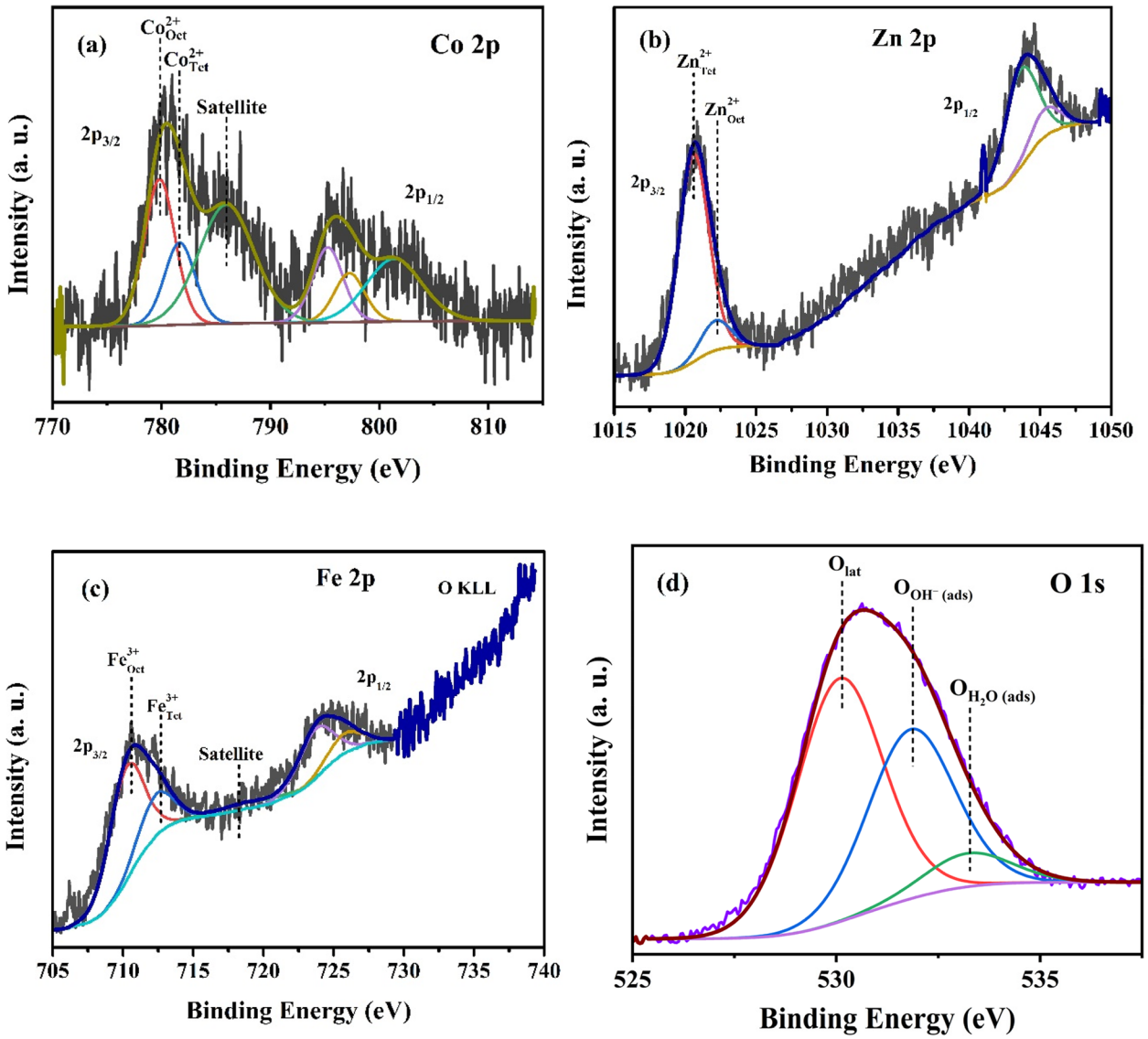

Fig. 7 Co 2p, Zn 2p, Fe 2p, and O 1s core level spectra in CZF

helpful details about the exchange of cations in ferrite materials.

Broad Co 2p, Zn 2p, Fe 2p, and O 1s core level spectra of CZF are decomposed into their component peaks by curve fitting as presented in Fig. 7. With a characteristic satellite peak at 785.4 eV displayed in Fig. 7a, the Co $2p_{3/2}$ peaks at 779.8 and 781.6 eV in the Co 2p core level spectra of CZF are assigned to Co^{2+} species in octahedral coordination and tetrahedral coordination, respectively, in the $CoFe_2O_4$ spinel structure [42, 46]. The areas under the corresponding decomposed peaks are used to estimate the relative surface concentrations of Co species related to the octahedral and tetrahedral coordination. It has been calculated that 64% Co^{2+} is found to be in octahedral sites, whereas 36% is in tetrahedral sites. Curve-fitted Zn 2p core level spectrum in CZF is displayed in Fig. 7b. Zn^{2+} species in tetrahedral site is indicated by the intense Zn $2p_{3/2}$ component peak at 1020.8 eV. Zn^{2+} species in octahedral site is responsible for the weak peak at 1022.0 eV. Relative concentrations of octahedral and tetrahedral Zn^{2+} species estimated from the spectrum are 16% and 84%, respectively. Figure 7c displays curve-fitted Fe 2p core level spectrum. Fe $2p_{3/2}$ peaks at 710.3 and 712.7 eV in the curve-fitted Fe 2p core level spectra, together with a distinctive weak satellite peak at 717.1 eV are indicative of octahedral and tetrahedral Fe^{3+} species [42]. Related satellite peak for Fe $2p_{1/2}$ is overlapped with intense O KLL Auger peak

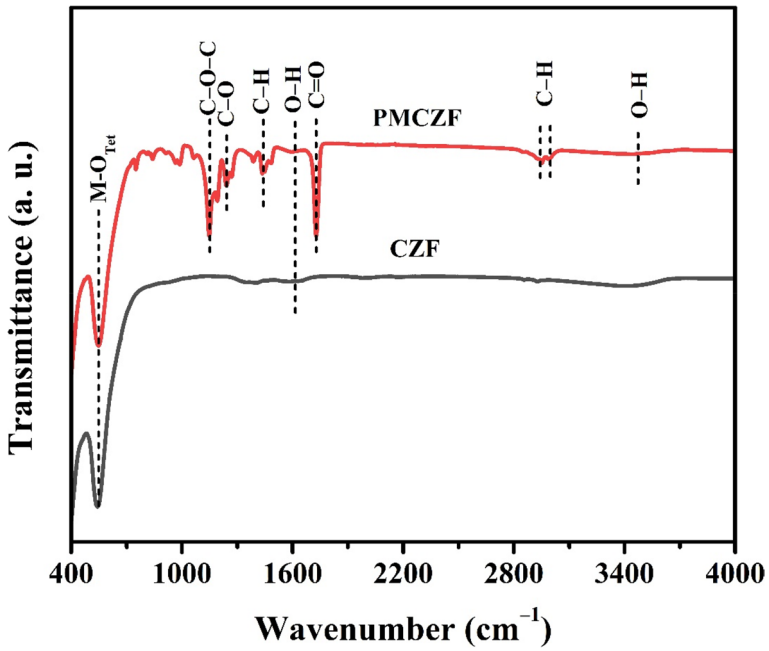

Fig. 8 FTIR spectra of CZF and PMCZF

as spectrum was recorded with MgKα radiation. Octahedral and tetrahedral Fe^{3+} entities have relative surface concentrations of 73% and 27%, respectively. Broad O 1s core level spectrum of CZF suggests the presence of several oxygen components. Curve-fitted O 1s core level spectrum is shown in Fig. 7d. The presence of Co, Fe, and Zn lattice oxygen species in CZF is indicated by the intense component peak at 530.1 eV. The hydroxyl (OH^-) and H_2O species adsorbed on the surface are responsible for the faint peaks that have been observed at 531.8 and 533.1 eV, respectively. The binding energy values of various oxygen species found in this study are in good accord with those available in earlier research for these kinds of species [42].

Relative surface concentrations of Co^{2+}, Zn^{2+}, and Fe^{3+} in their octahedral and tetrahedral sites from XPS data can be utilized to estimate the cation distribution in CZF. The estimated cation distribution in CZF is found to be $(Co^{2+}_{0.18}Zn^{2+}_{0.42}Fe^{3+}_{0.54})$ $[Co^{2+}_{0.32}Zn^{2+}_{0.08}Fe^{3+}_{1.46}]$.

FTIR spectroscopy studies

FTIR studies of the CZF and PMCZF have been conducted to figure out the nature of metal–oxygen bonding present in these materials and the spectra are shown in Fig. 8. Formation of a single phase AB_2O_4 spinel structure with A-site that is a divalent metal cation in tetrahedral coordination and B-site that is a trivalent metal cation in octahedral coordination is confirmed by IR bands seen in spinel ferrites below 1000 cm^{-1} [42]. Lattice vibrations of oxide ion against cations result in these bands. As per FTIR literature of spinel ferrites, the absorption band at higher wavenumber (ν_1) represents a metal–oxygen bond in tetrahedral sites, while the absorption band found at lower wavenumber (ν_2) embodies a metal–oxygen bond in octahedral sites. CZF and PMCZF exhibit a broad intense absorption band in the 500–600 cm^{-1} frequency region in the current study. The band broadening in inverse spinel ferrites is because of the statistical distribution of Co^{2+}, Zn^{2+}, and Fe^{3+} ions at A- and B-sites. As a result, the high wavenumber band is attributed to M↔O vibrations in tetrahedral sublattice site A, whereas the lower wavenumber band is assigned to M↔O vibrations in octahedral sublattice site B. An intense peak observed around 543.6 cm^{-1} in both ferrites is assigned to tetrahedral band position of M↔O vibrations such as Co–O, Zn–O, and Fe–O [42]. However, C–O–C, C–O, C–H, and C=O stretching bands at 1147, 1242, 1442, and 1723 cm^{-1} are noticed in PMCZF. Asymmetric stretching of C–H bond is related to the observed bands at 2949 and 2999 cm^{-1} [47]. These additional peaks are seen in the PMCZF sample corresponding to the presence of PMMA. However, in both samples, peaks related to C–H bond are found at 1614 and 3473 cm^{-1}.

Dependency of vibrational frequencies of spinel ferrites on cation mass, cation–oxygen bonding force, cation–oxygen bond length, and cation distribution is well established in the literature. In general, the vibrational frequency of a bond is related to the mass of the system and the force constant of the bond. From classical

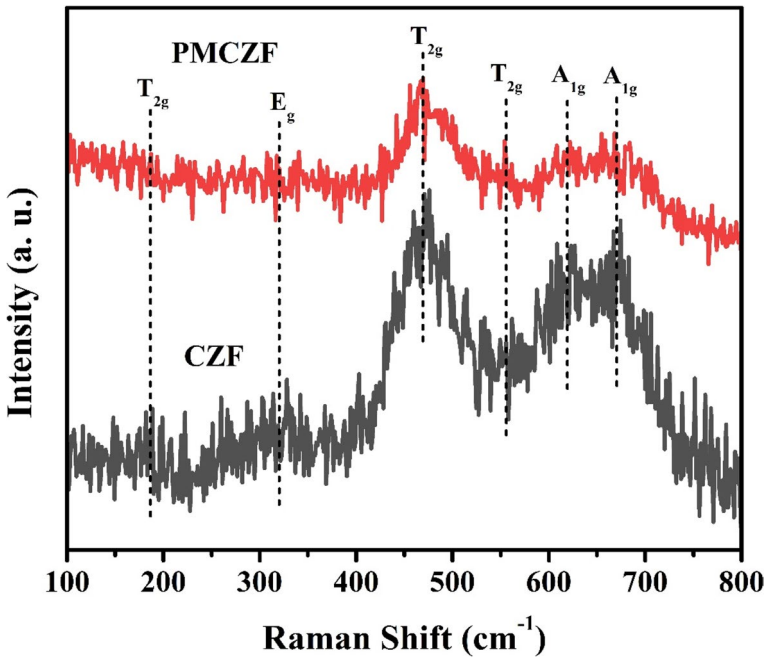

Fig. 9 Raman spectra of CZF and PMCZF

physics, Hooke's law represents vibrational frequency ($\bar{\nu}$) in wavenumber (cm^{-1}) of a bond as written below [42]:

$$\bar{\nu} = \frac{1}{2\pi c}\sqrt{\frac{k}{\mu}} \tag{3}$$

where k is force constant of the bond related to its strength, μ is reduced mass of the bond, and c is velocity of light. Reduced mass is written by the relation:

$$\mu = \frac{m_1 m_2}{m_1 + m_2} \times u \tag{4}$$

where m_1 and m_2 are masses of atoms involved in the vibration and u is unit mass (1.6605×10^{-24} g). Further, force constant is calculated by reorganizing the Eq. (3) as given below:

$$k = 4\pi^2 c^2 \bar{\nu}^2 \mu \tag{5}$$

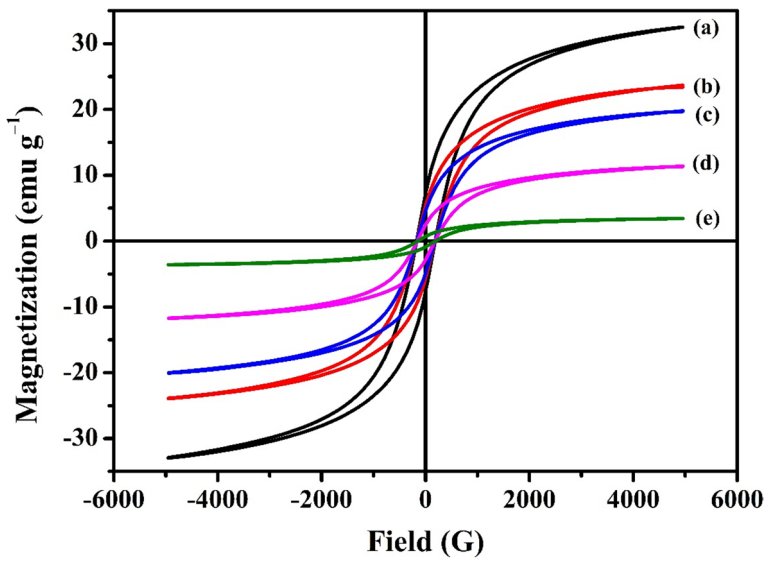

Fig. 10 M–H curves of PMCZF–PANI composites: (**a**) PMCZF, (**b**) PMCZF–PANI 73, (**c**) PMCZF–PANI 55, (**d**) PMCZF–PANI 37, and (**e**) PMCZF–PANI 19

Therefore, from observed band positions ($\overline{\nu}$), c (3×10^{10} cm s^{-1}), and μ, force constants associated with the bands having tetrahedral and octahedral coordinations can be computed. Here, m_1 and m_2 are weighted average of atomic mass of cations residing at A-site (tetrahedral) or B-site (octahedral) and atomic mass of oxide ion, respectively, which are used to calculate the μ. In this work, tetrahedral force constants (k_{Tet}) are calculated due to clarity of tetrahedral band positions of the ferrites in the recorded spectral range. Because of unclarity of corresponding band positions their octahedral force constants (k_{Oct}) are not estimated. Observed k_{Tet} value of is 2.257×10^5 dyn cm^{-1} (225.7 N m^{-1}).

Raman spectroscopy studies

Structural distortion and oxygen motion in spinel structure can be understood using Raman spectroscopy. Space group of $Fd\,\overline{3}\,m$ (O^7_h, Space Group # 227) represents the crystalline cubic ferrite materials. There are 56 atoms (Z = 8) in complete unit cell and only 14 atoms (Z = 2) in the smallest Bravais cell. Thus, 42 vibrational modes are conceivable due to 42 degrees of freedom. Of the 42 modes, 39 are associated with optical modes, and the other three corresponds to acoustic modes. Group theoretical analysis indicates that the spinel structure has 17 sets of phonon modes at the Γ-point of the Brillouin zone in spinel structure [42, 46]. Out of these vibrational modes, 5 modes are Raman-active. Of the remaining, 4 vibrational modes are infrared-active, 7 modes are silent, and 1 mode is acoustic modes. The motions of O ions and both A-site and B-site ions in the spinel structure are associated with Raman active modes. In spinel structure, the metal cations surrounded by six oxygen and by four oxygen ions form an octahedron and a tetrahedron, respectively. The A_{1g} mode corresponds to symmetric stretching of the oxygen anion, the E_g mode is related to symmetric bending of the oxygen anion, and the T_{2g} mode is associated with asymmetric stretching of the oxygen anion.

Figure 9 represents Raman spectra of CZF and PMCZF. Literature states that oxygen motion around the octahedral lattice sites is responsible for low frequency vibrations (below 600 cm^{-1}), while oxygen motion around the tetrahedral sites is responsible for high frequency vibrations. The shorter is the bond length and thus, higher is the vibrational frequencies, thereby smaller is the coordination number (4 for tetrahedral sites and 6 for octahedral ones). The spectra illustrate Raman modes at 190, 325, 470, 555, 610, and 685 cm^{-1}. $A1_g$ modes which represents the symmetry stretching vibrations of the Fe–O and Zn–O bonds in tetrahedral sites, are associated with Raman modes at around 685 cm^{-1} and 610 cm^{-1}. T_{2g} and E_g Raman modes, which are related to vibration of Fe–O and Zn–O bonds in octahedral sites of the spinel structure, correspond to the lower frequency modes observed at 190, 325, 470, and 550 cm^{-1}.

Magnetic properties

Change in magnetization or magnetic flux of the material in response to an applied field is represented by magnetization curve. A material containing randomly oriented magnetic moments will gradually become magnetized when a field is applied because of the movement of domain boundaries. $Co_{0.5}Zn_{0.5}Fe_2O_4$ is a widely recognized magnetic material characterized by moderate magnetization and high coercivity. Its cubic spinel structure (AB_2O_4) comprises two separate sub lattices and vacant B site that gives rise to the ferromagnetic ordering in the material. On the other hand, spins of metal cations at the tetrahedral (A) and octahedral (B) sites in spinel ferrites interact magnetically through the mediation of oxygen ions which is termed as superexchange mechanism. As per the sublattice model, the difference between the sum of the magnetic moments of octahedral (M_B) and tetrahedral (M_A) sublattices ($M = M_B - M_A$) determines the net magnetization in spinel ferrites. Ferrimagnetic ordering is the magnetization which is because of strong antiferromagnetic interaction between AB pairs. Figure 10 shows magnetic hysteresis loops (M–H curves) of different PMCZF–PANI composites. Magnetization rises as the applied field is increased in each case. Hysteresis loops provide saturation magnetization (M_s), remanence or remanent magnetization (M_r), coercivity (H_c) and remanence or remanent or squareness ratio (M_r/M_s) values

Table 2 Saturation magnetization (M_s), remanent magnetization (M_r), coercivity (H_c), remanence ratio (M_r/M_s), and magnetic moment (μ_B) of $Co_{0.5}Zn_{0.5}Fe_2O_4$–PANI composites

Sample	M_s (emu g^{-1})	Mr (emu g^{-1})	Mr/M_s	H_c (G)	μ_B (BM)
PMCZF	32.5	7.2	0.22	358	1.1
PMCZF – PANI 73	23.8	5.5	0.23	357	0.8
PMCZF – PANI 55	19.8	4.6	0.23	357	0.7
PMCZF – PANI 37	11.5	2.6	0.22	357	0.4
PMCZF – PANI 19	3.5	0.7	0.21	345	0.1

which are presented in Table 2. Magnetic moments of these composites are computed from their respective M_s values according to the equation given below [41]:

$$\mu_B = \frac{Molecular\ weight}{5585} \times M_s \tag{6}$$

where μ_B is magnetic moment and M_s is saturation magnetization. Calculated values of magnetic moment are also included in Table 2. Saturation magnetization (M_s) of PMCZF is 32.5 emu g^{-1} with coercive field of 358 G. It is to be noted that as PANI concentration rises, magnetization value decreases. Saturation magnetization value drops to 23.8 emu g^{-1} with coercive field of 357 G at 30 wt% PANI concentration.

The low saturation magnetization of the PMCZF−PANI composites compared to CZF is because of nonmagnetic PANI is mixed with different amounts. Nonetheless, all samples show almost same coercivity values. Coercivity of magnetic a material is determined by the number and strength of magnetic dipole within magnetic domains as well as the interactions between neighboring magnetic domains. Therefore, it results in less effect on the coercivity of PMCZF in PMCZF−PANI composites. From these results, it is clear that PMCZF−PANI composites are ferromagnetic in nature and can be good absorbers of EM wave in GHz range.

EMI shielding properties

The ability of a material to block or attenuate EM waves is referred to as EMI shielding and material is called EMI shielding material. Three basic interaction phenomena such as reflection, transmission, and absorption occur when incident EM wave falls on the EMI shielding material. The incident power (P_i) of EM wave is divided into three parts: (a) reflected power (P_r) on the front and rear surfaces, (b) transmitted power (P_t) outside the shielding material, and (c) absorbed power (P_a) in propagation. Three coefficients comprising reflection (R), transmission (T), and absorption (A) are used to quantify the shielding effectiveness with respect to the weakening of EM power (P), electric field intensity (E), and magnetic field intensity (H). Generally, each of the coefficients varies in the range of 0−1 and sum of them is equal to 1 as given below:

$$R + T + A = 1 \tag{7}$$

From the above equation it is clear that larger the values of R and A, lower will be the value of T. The coefficients are written as follows [6]:

$$R = \frac{P_r}{P_i} = \left|\frac{E_r}{E_i}\right|^2 = \left|\frac{H_r}{H_i}\right|^2 \tag{8}$$

$$T = \frac{P_t}{P_i} = \left|\frac{E_t}{E_i}\right|^2 = \left|\frac{H_t}{H_i}\right|^2 \tag{9}$$

$$A = \frac{P_a}{P_i} = \left|\frac{E_a}{E_i}\right|^2 = \left|\frac{H_a}{H_i}\right|^2 = 1 - R - T \tag{10}$$

where P_i, E_i, and H_i are electromagnetic power, electric field intensity, magnetic field intensity incident on the shielding material, P_t, E_t, and H_t are the same transmitted through the shielding material, and P_a, E_a, and H_a are the same absorbed through the shielding material.

Generally, EMI shielding of a material is expressed in terms of overall shielding effectiveness or overall loss (SE) and its unit is decibel (dB). A higher SE value indicates less energy transmitted through the shielding material, where most of the radiation is either reflected or absorbed by the shielding material. Therefore, EM wave attenuation occurs through reflection, absorption, and multiple reflection mechanisms. The attenuation through reflection of EM wave is governed by surface reflection (SE_R) from free charge carriers in the system and by multiple reflections (SE_{MR}) from adjacent conducting layers. In contrast, the attenuation through absorption (SE_A) of EM wave is governed by several loss mechanisms associated with electric polarization and magnetization processes [48]. The amount of EM wave reduction is determined by the materials chosen, their thickness, the size of the shielded volume, and the frequency of the fields of interest. SE of a material is a ratio of the incident energy to the residual energy. It is a function of the logarithm ratio of incident radiation power to the transmitted power and generally written as [41, 49]:

$$SE = -10\log\frac{P_t}{P_i} = -20\log\frac{E_t}{E_i} = -20\log\frac{H_t}{H_i} \tag{11}$$

According to Schelkunoff's theory, SE is the sum of SE_R, SE_A, and SE_{MR} which is expressed as:

$$SE = SE_R + SE_A + SE_{MR} \tag{12}$$

The attenuation of EM wave from multiple reflections is not as high as the ones due to absorption and reflection. In the view of this, its value is negligible and can be written as:

$$SE_{MR} = 20\log\left(1 - e^{-\frac{2t}{\delta}}\right) = 20\log\left(1 - 10^{-\frac{SE_A}{10}}\right) \tag{13}$$

where t, δ, and e are thickness and skin depth of shielding material, and Napier's constant or Euler's number (2.718), respectively. According to this equation, for a material with high SE_A value, S_{MR} value will be very low.

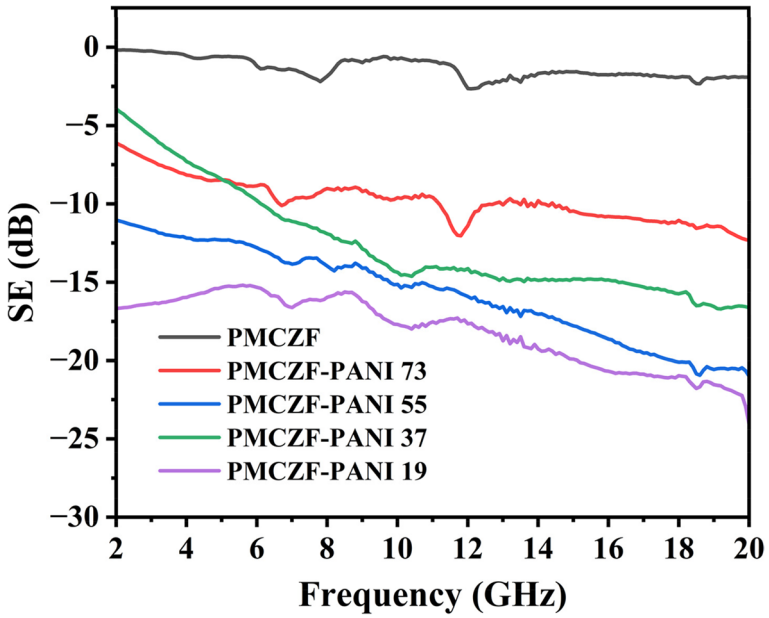

Fig. 11 SE of PMCZF–PANI composites as a function of frequency

Table 3 SE values of various composites in at 2–20 GHz frequency region

Sample	SE (dB)
PMCZF	−0.1 to −1.8
PMCZF–PANI 73	−6.2 to −12.3
PMCZF–PANI 55	−11.1 to −20.8
PMCZF–PANI 37	−3.9 to −16.5
PMCZF–PANI 19	−16.6 to −24.2

Generally, S_{MR} term is neglected when $SE_A \geq -10$ dB [49]. Because of absorption, while moving from one boundary to another the magnitude of EM waves is neglected at high frequencies. Materials with a high ability of absorption and high thickness can neglect safely multiple/internal reflections. Also, according to Schelkunoff's shielding theory, SE_{MR} can be neglected when $t > \delta$. Multiple reflections depend on the thickness relationship between skin depth and distance from reflection to interface. It is to be noted that EM wave at high frequencies penetrates only the near surface region of an electrical conductor. This is regarded as skin effect. The electric field of incident EM wave decreases exponentially when it passes through the conductor. The depth at which the field falls to 1/e of the incident value is called the skin depth (δ). It is an important property of the material to understand the propagation of EM waves that can pass through the shielding material. It is determined by using the parameters like frequency (f), electrical conductivity (σ), and magnetic permeability (μ) and is written as [49, 50]:

$$\delta = \frac{1}{\sqrt{\pi f \sigma \mu}} = -8.68\left(\frac{t}{SE_A}\right) \tag{14}$$

Hence, the skin depth decreases with increasing frequency, conductivity or permeability. Therefore, for RAM or stealth applications, shielding due to reflection is undesirable and thus, achieving SE only due to SE_A becomes a challenging task.

In recent days, VNA has widely been utilized to measure shielding effectiveness of EMI shielding materials by waveguide method and coaxial transmission line method. With the two-port VNA, reflection and transmission coefficients can be measured in terms of scattering parameters (S-parameters) consisting of S_{11} (forward reflection coefficient) and S_{12} (reverse transmission coefficient) and their reciprocals such as S_{22} (reverse reflection coefficient), and S_{21} (forward transmission coefficient). The samples are bombarded by EM waves from both sides and S-parameters are obtained from VNA. The S-parameters are written as [6]:

$$R = \left|\frac{E_r}{E_i}\right|^2 = |S_{11}|^2 = |S_{22}|^2 \tag{15}$$

$$T = \left|\frac{E_t}{E_i}\right|^2 = |S_{12}|^2 = |S_{21}|^2 \tag{16}$$

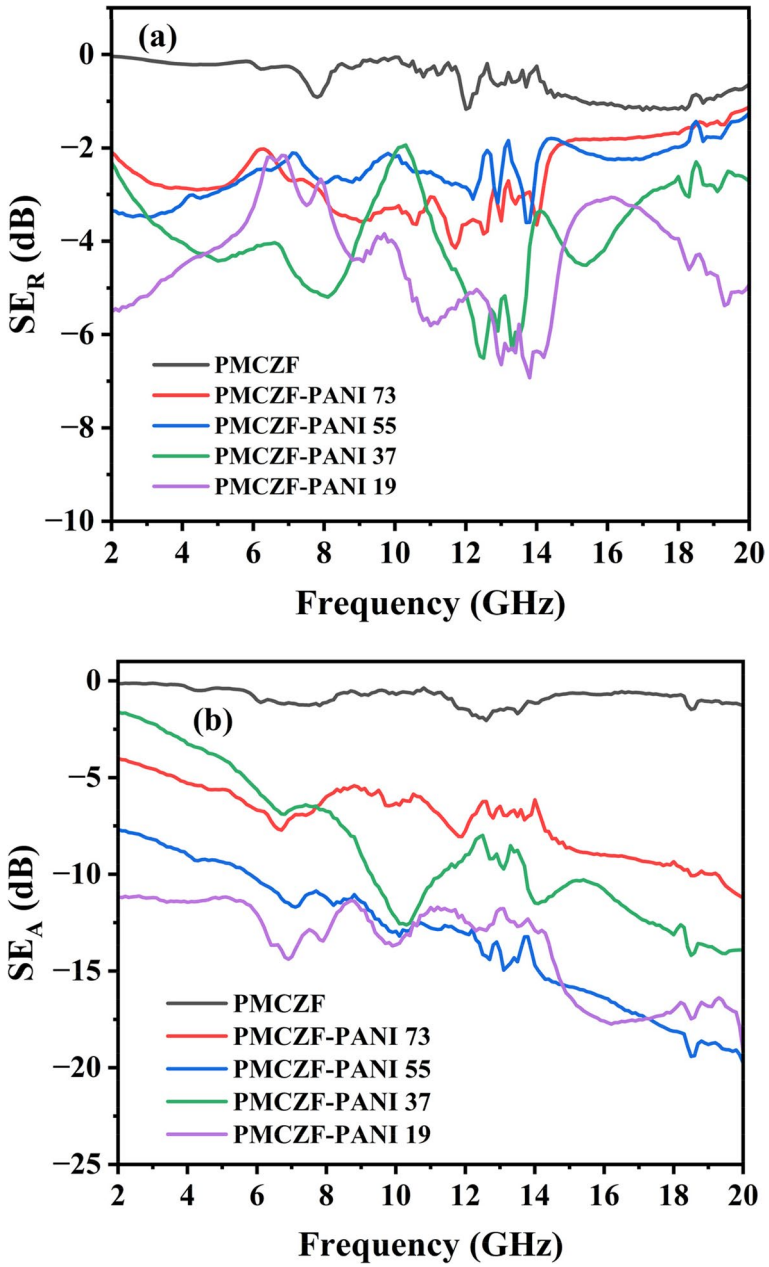

Fig. 12 Plots of (**a**) SE_R and (**b**) SE_A of PMCZF–PANI composites as a function of frequency

Considering multiple reflection effect as negligible when $SE_A \geq -10$ dB, relative intensity of effective EM wave inside the material after reflection will be 1−R and therefore, effective absorbance (A_{eff}) is described as:

$$A_{eff} = \frac{1 - R - T}{1 - R} = \frac{A}{1 - R} \tag{17}$$

The shielding effectiveness through reflection (SE_R) and shielding effectiveness through absorption (SE_A) are related to the reflection and transmission coefficients in the following way:

$$SE_R = -10\log(1 - R) \tag{18}$$

$$SE_A = -10\log(1 - A_{eff}) = -10\log\frac{T}{1 - R} \tag{19}$$

The total shielding effectiveness (SE) consists of contributions from SE_R and SE_A. Therefore, SE, SE_R, and SE_A

Table 4 Maximum SE values of different polyaniline (PANI)-based composites

Composite	SE (dB) (Frequency range)	Reference
PANI/CFO@CNTs	−16.8 (8–12 GHz)	5
PANI/MXene/CF	−26 (8–12 GHz)	51
PANI/MXene	−35.3 (8–12 GHz)	52
PANI-MoO_3	−14.0 (8–12 GHz)	53
PANI/GRNP	−14.5 (8–12 GHz)	54
$CoFe_2O_4$–PANI	−22.8 (8–12 GHz)	55
PMCZF–PANI 55	−20.8 (2–20 GHz)	This work
PMCZF–PANI 19	−24.2 (2–20 GHz)	This work

can be expressed in terms of S-parameters employing following equations [26]:

$$SE = SE_R + SE_A = -10\log(1-R) - 10\log\frac{T}{1-R} = -10\log T \quad (20)$$

$$SE = -10\log|S_{12}|^2 = -10\log|S_{21}|^2 \quad (21)$$

$$SE_R = -10\log(1-|S_{11}|^2) = -10\log(1-|S_{22}|^2) \quad (22)$$

$$SE_A = -10\log\left(\frac{|S_{12}|^2}{1-|S_{11}|^2}\right) = -10\log\left(\frac{|S_{21}|^2}{1-|S_{22}|^2}\right) \quad (23)$$

In the present study, EMI shielding properties of PMCZF–PANI composites with different concentration ratios have been carried out for the optimization of composite by coaxial method. Plots of SE values of PMCZF–PANI composites as a function of frequency are presented in Fig. 11. The values at 2–20 GHz for all the samples are summarized in Table 3. It is clear from the table that EMI shielding performance of the composites can be tuned to the desired values with changing the weight ratio of ferrite and PANI. All composites show SE values higher than 10 dB in higher frequency region. Particularly, PMCZF–PANI 55 and PMCZ–PANI 19 composites with 50 wt% and 90 wt% PANI show the values in the range of −11.1 to −20.8 dB and −16.6 to −24.2, respectively. The SE of PMCZF–PANI 19 composite have highest SE value of −24.2 dB. It is to be noted that absorption and reflection components of shielding effectiveness are valuable indicators of the shielding mechanism of the composites. Plots of SE_R and SE_A values of PMCZF–PANI composites as a function of frequency are shown in Fig. 12. From the figure it is understood that SE_R values are found to be low in the entire frequency range, whereas maximum SE_A values of PMCZF–PANI 73, 55, 37, and 19 composites are observed to be −11.1, −20.1, −13.9, and −17.3 dB, respectively. These findings suggest that the shielding mechanism of PMCZF–PANI composites is dominated by the absorption component. The observed SE values in PMCZF–PANI 55, and 19 composites are observed to > −20 dB in the higher frequency region of 13–20 GHz indicating that these composites can be useful for EMI shielding applications in higher frequency region. Table 4 represents a comparison of the total shielding effectiveness of representative PANI-based composite materials with PMCZF–PANI composites studied in the present work [5, 51–55].

According to the Eq. (14), skin depths of these composite materials have been calculated from t and SE_A values in the frequency range of 2–20 GHz which is presented in Fig. 13. From the figure it is clear that skin depth values of the composites especially, PMCZF–PANI 55, PMCZF–PANI 37, and PMCZF–PANI 19 decrease with increase in frequency.

Furthermore, morphology of the EMI shielding materials plays an important role because of their excellent shielding performance and its tunability. The existence of pores, voids, and channels in the materials results in a variety of phenomena, including diffraction, reflection, and scattering of incident EM waves, prolonging the interaction time and the distance over which the EM waves interact with molecules or particles of the material. This enhances multiple reflection, thereby improving the absorption of EM waves [48, 56, 57]. In the present study, PMCZF materials in PMCZF–PANI-based EMI shielding materials contain voids and have good magnetic properties. Again, one of the constituents of the composites is conducting polymer, PANI. Therefore, the composites containing PMCZF with PANI show excellent EMI shielding effectiveness properties.

Conclusions

$Co_{0.5}Zn_{0.5}Fe_2O_4$ spinel ferrite has been prepared by SCS method and this ferrite has been modified using PMMA. Oxidative chemical polymerization has been used to prepare PANI in the laboratory. Ferrites adopt cubic spinel structure as demonstrated by XRD studies. Porous and agglomerated morphologies of the ferrites

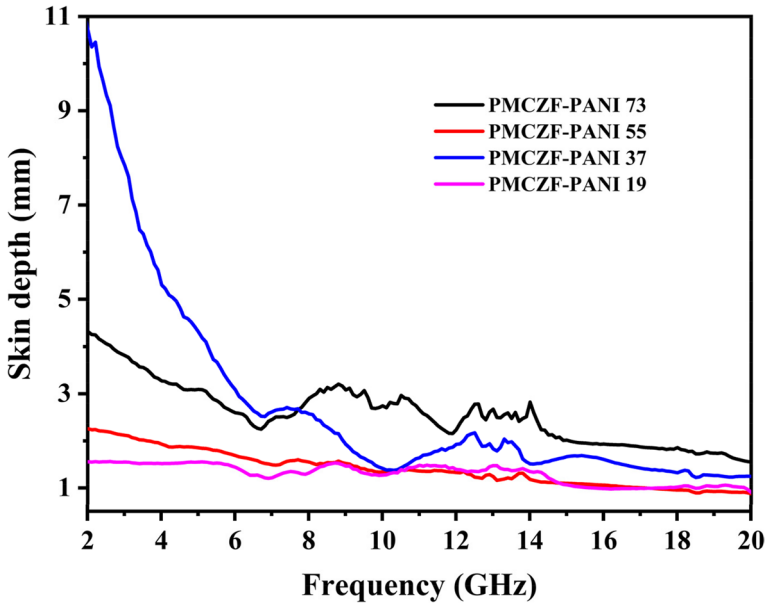

Fig. 13 Skin depth of PMCZF–PANI composites with respect to frequency

have been revealed by FESEM investigation. HRTEM image of as-prepared ferrite shows highly ordered lattice fringes with *d*-spacing of 2.56 Å corresponding to (311) lattice plane of the $Co_{0.5}Zn_{0.5}Fe_2O_4$ spinel structure. XPS studies have demonstrated the presence of tetrahedral and octahedral Co^{2+}, Fe^{3+}, and Zn^{2+} species in $Co_{0.5}Zn_{0.5}Fe_2O_4$. FTIR and Raman studies show the presence of metal–oxygen bonds in the ferrites. Their magnetic and EMI properties have been studied. With increase in PANI concentrations saturation magnetization of these composite materials decreases. PMCZF–PANI 73 show the M_s value of 23.8 emu g^{-1} with 30% PANI. PMCZF–PANI 19 composite shows total absorption of − 16.6 to − 24.2 dB in the 2–20 GHz frequency range. In all the composites, absorption component dominates. As SE values are higher than −20 dB in the frequency > 13 GHz in PMCZF–PANI 55 and PMCZF–PANI 19 composites they can be used in higher frequency application. Skin depth values are observed to decrease with increase in frequency.

Acknowledgements
Authors thank Director, CSIR–National Aerospace Laboratories, Bengaluru for financial assistance and his constant support for carrying out this work. Authors wish to thank Mr. G. Srinivas, Mr. Siju John, Ms. S. Latha, and Dr. Prasanta Chowdhury for XRD, FESEM, XPS, and magnetic measurements, respectively.

Author's contribution
PB, RVL, and RPSC prepared the materials and performed characterization. SB carried out EMI measurements. HCB contributed the funding, project administration, and resources. PB analyzed data and wrote the original manuscript. All authors reviewed the manuscript.

Availability of data and materials
No datasets were generated or analysed during the current study.

Declarations

Competing interests
The authors declare no competing interests.

Author details
[1]Surface Engineering Division, CSIR–National Aerospace Laboratories, Bengaluru 560017, India. [2]Department of Materials Engineering, Indian Institute of Science, Bengaluru 560012, India.

Received: 31 January 2024 Accepted: 10 June 2024
Published online: 09 September 2024

References

1. A. Rayar, C.S. Naveen, H.S. Onkarappa, V.S. Betageri, G.D. Prasanna, EMI shielding applications of PANI-Ferrite nanocomposite materials: A review. Synth. Met. **295**, 117338 (2023)
2. M. Zahid, R. Anum, S. Siddique, H.M.F. Shakir, Z.A. Rehan, Polyaniline-based nanocomposites for electromagnetic interference shielding applications: A review. J. Thermoplast. Compos. Mater. **36**, 1717–1761 (2023)
3. S.S. Chauhan, M. Abraham, V. Choudhary, Electromagnetic shielding and mechanical properties of thermally stable poly(ether ketone)/multi-walled carbon nanotube composites prepared using a twin-screw extruder equipped with novel fractional mixing elements. RSC Adv. **6**, 113781–113790 (2016)
4. S. Akram, M. Ashraf, A. Javid, H.A. Abid, S. Ahmad, Y. Nawab, A. Rasheed, Z. Xue, A. Nosheen, Recent advances in electromagnetic interference (EMI) shielding textiles: A comprehensive review. Synth. Met. **294**, 117305 (2023)
5. S.J. Kazmi, M. Nadeem, A. Younis, S. Loomba, B. Shabbir, S. Manzoor, S. Hussain, PANI/CFO@CNTs ternary composite system for EMI shielding applications. J. Magn. Magn. Mater. **563**, 170037 (2022)
6. X. Jia, Y. Li, B. Shen, W. Zheng, Evaluation, fabrication and dynamic performance regulation of green EMI-shielding materials with low reflectivity: A review. Compos Part B **233**, 109652 (2022)
7. D.D.L. Chung, Materials for electromagnetic interference shielding. Mater. Chem. Phys. **255**, 123587 (2020)
8. M. Qin, L. Zhang, H. Wu, Dielectric loss mechanism in electromagnetic wave absorbing materials. Adv. Sci. **9**, 2105553 (2022)

9. S.T. Maleki, M. Babamoradi, Microwave absorption theory and recent advances in microwave absorbers by polymer-based nanocomposites (carbons, oxides, sulfides, metals, and alloys). Inorg. Chem. Commun. **149**, 110407 (2023)
10. F. Ruiz-Perez, S.M. López-Estrada, R.V. Tolentino-Hernández, F. Caballero-Briones, Carbon-based radar absorbing materials: A critical review. J. Sci.: Adv. Mater. Devices **7**, 100454 (2022)
11. H. Abbasi, M. Antunes, J.I. Velasco, Recent advances in carbon-based polymer nanocomposites for electromagnetic interference shielding. Prog. Mater. Sci. **103**, 319–373 (2019)
12. M. Green, X. Chen, Recent progress of nanomaterials for microwave absorption. J. Materiomics **5**, 503–541 (2019)
13. R. Peymanfar, H. Dogari, E. Selseleh-Zakerin, M.H. Hedayatzadeh, S. Daneshvar, N. Amiri-Ramsheh, H. Ghafuri, A. Mirkhan, G. Ji, B. Aslibeiki, Recent advances in microwave-absorbing materials fabricated using organic conductive polymers. Front. Mater. **10**, 1133287 (2023)
14. L. Lyu, J. Liu, H. Liu, C. Liu, Y. Lu, K. Sun, R. Fan, N. Wang, N. Lu, Z. Guo, E.K. Wujcik, An overview of electrically conductive polymer nanocomposites toward electromagnetic interference shielding. Eng. Sci. **2**, 26–42 (2018)
15. G.P. Abhilash, K. Sushmita, S. Bose, C. Shivakumara, Functionalization of dielectric $BaTiO_3$ and semiconducting ZnO nanoparticles on rGO layers and their polymer composites: Applications in EMI shielding. Synth. Met. **297**, 117387 (2023)
16. K. Sushmita, G. Madras, S. Bose, Polymer nanocomposites containing semiconductors as advanced materials for EMI shielding. ACS Omega **5**, 4705–4718 (2020)
17. R.V. Lakshmi, P. Bera, E.V. Bhavya, B. Choudhury, N.K. Namdeo, A.K. Kundu, H.C. Barshilia, Microwave absorbing and dielectric properties of GaN. J. Electron. Mater. **52**, 6492–6502 (2023)
18. L. Zhang, Y. Lv, X. Ye, L. Ma, S. Chen, Y. Wu, Q. Wang, Polypyrrole decorated flower-like and rod-like ZnO composites with improved microwave absorption performance. Materials **15**, 3408 (2022)
19. H. Su, B. Luan, Y. Dong, X. Zhang, Z. Liu, C. Wang, Lotus leaf-like Ni-decorated SiC with combined superhydrophobicity and enhanced microwave absorption performance. Colloids Surf. A **650**, 129602 (2022)
20. T. Chakraborty, S. Sharma, K. Das, A.S. Mahapatra, A. Saha, S. Das, S. Saha, S. Chakrabarti, S. Das, S. Sutradhar, Shielding effectiveness study of CoZCF-MWCNT nanocomposite materials and its possible application as EM pollution reducer. Phys. Scr. **98**, 065914 (2023)
21. S. Parmar, B. Ray, S. Garg, R.K. Mishra, S. Datar, Reduced graphene oxide (rGO)-ferrite composite inks and their printed meta-structures as an adaptable EMI shielding material. Compos. Interfaces **30**, 301–321 (2023)
22. K.A. Darwish, O.M. Hemeda, M.I.A. Ati, A.S.A. El-Hameed, D. Zhou, M.A. Darwish, M.M. Salem, Synthesis, characterization, and electromagnetic properties of polypyrrole–barium hexaferrite composites for EMI shielding applications. Appl. Phys. A **129**, 460 (2023)
23. J. Zhang, Y. Liu, Z. Liao, J. Hu, A. Ma, Y. Ma, C. Feng, M. Ma, MoS_2-based materials for microwave absorption: An overview of recent advances and prospects. Synth. Met. **291**, 117188 (2022)
24. F. Wang, C. Bai, L. Chen, Y. Yu, Boron nitride nanocomposites for microwave absorption: a review. Mater. Today Nano. **13**, 100108 (2021)
25. M. Green, Z. Liu, P. Xiang, X. Tan, F. Huang, L. Liu, X. Chen, Ferric metal-organic framework for microwave absorption. Mater. Today Chem. **9**, 140–148 (2018)
26. J. Kruželák, A. Kvasničáková, K. Hložeková, I. Hudec, Progress in polymers and polymer composites used as efficient materials for EMI shielding. Nanoscale Adv. **3**, 123–172 (2021)
27. D. Parajuli, S. Uppugalla, N. Murali, A. Ramakrishna, B. Suryanarayana, K. Samatha, Synthesis and characterization MXene-ferrite nanocomposites and its application for dying and shielding. Inorg. Chem. Commun. **148**, 110319 (2023)
28. M. Chang, Q. Li, Z. Jia, W. Zhao, G. Wu, Tuning microwave absorption properties of $Ti_3C_2T_x$ MXene-based materials: Component optimization and structure modulation. J. Mater. Sci. Technol. **148**, 150–170 (2023)
29. M. Kallumottakkal, M.I. Hussein, M.Z. Iqbal, Recent progress of 2D nanomaterials for application on microwave absorption: A comprehensive study. Front. Mater. **8**, 633079 (2021)
30. A. Iqbal, P. Sambyal, C.M. Koo, 2D MXenes for electromagnetic shielding: A review. Avd. Funct. Mater. **30**, 2000883 (2020)
31. L. Xu, Z. Lin, Y. Chen, Z. Fan, X. Pei, S. Yang, X. Kou, Y. Wang, Z. Zou, D. Xi, P. Yin, G. Su, M. Zhou, J. Dai, L. Pan, Y. Zhao, Carbon-based cages with hollow confined structures for efficient microwave absorption: State of the art and prospects. Carbon **201**, 1090–1114 (2023)
32. K. Ren, Y. Wang, C. Ye, Z. Du, J. Bian, C. Long, S. Zhao, W. Li, J. Guan, Realizing significant dielectric dispersion of composites based on highly conducting silver-coated glass microspheres for wide-band non-magnetic microwave absorbers. J. Mater. Chem. C **7**, 528–542 (2019)
33. X. Cai, H. Guo, H. Zhu, D. Yin, H. Guo, D. Bi, K. Yu, H. Yang, J. Pan, Effect of cooling medium on the preparation and microwave absorption properties in low frequency for LiZn ferrites hollow microspheres. J. Alloys Compd. **906**, 164290 (2022)
34. D. Mandal, K. Mandal, Electromagnetic wave attenuation properties of MFe_2O4 (M = Mn, Fe Co, Ni, Cu, Zn) nano-hollow spheres in search of an efficient microwave absorber. J. Magn. Magn. Mater. **536**, 168127 (2021)
35. D. Kumar, A. Moharana, A. Kumar, Current trends in spinel based modified polymer composite materials for electromagnetic shielding. Mater. Today Chem. **17**, 100346 (2020)
36. N. Gulzar, K. Zubair, M.F. Shakir, M. Zahid, Y. Nawab, Z.A. Rehan, Effect on the EMI shielding properties of cobalt ferrites and coal-fly-ash based polymer nanocomposites. J. Supercond. Novel Magn. **33**, 3519–3524 (2020)
37. I. Ahmad, M. Zeshan, M.M. Alanazi, S.A. Abdelmohsen, H.F.T. Farid, Study of $CoCe_{0.05}Fe_{1.95}O_4$-polypyrrole composite for efficient electromagnetic interference shielding. Curr. Appl. Phys. **51**, 64–70 (2023)
38. M. Chahar, V. Sharma, O.P. Thakur, Conductive network structure of MWCNTs-incorporated cobalt-zinc ferrite nanocomposite for enhanced electromagnetic shielding applications. J. Nanopart. Res. **24**, 195 (2022)
39. J. Sun, L. Wang, Q. Yang, Y. Shen, X. Zhang, Preparation of copper-cobalt-nickel ferrite/graphene oxide/polyaniline composite and its applications in microwave absorption coating. Prog. Org. Coat. **141**, 105552 (2020)
40. R. Kuekha, T.H. Mubarak, B. Azhdar, Electromagnetic interference shielding and characterization of Ni^{2+} substituted cobalt nanoferrites prepared by sol-gel auto combustion method. Adv. Mater. Sci. Eng. **2022**, 3992402 (2022)
41. R.V. Lakshmi, P. Bera, R.P.S. Chakradhar, B. Choudhury, S.P. Pawar, S. Bose, R.U. Nair, H.C. Barshilia, Enhanced microwave absorption properties of PMMA modified $MnFe_2O_4$–polyaniline nanocomposites. Phys. Chem. Chem. Phys. **21**, 5068–5077 (2019)
42. P. Bera, R.V. Lakshmi, B.H. Prakash, K. Tiwari, A. Shukla, A.K. Kundu, K. Biswas, H.C. Barshilia, Solution combustion synthesis, characterization, magnetic, and dielectric properties of $CoFe_2O_4$ and $Co_{0.5}M_{0.5}Fe_2O_4$ (M = Mn, Ni, and Zn). Phys. Chem. Chem. Phys. **22**, 20087–20106 (2020)
43. K.C. Patil, M.S. Hegde, T. Rattan, S.T. Aruna, Chemistry of nanocrystalline oxide materials: Combustion synthesis properties and applications (World Scientific, Singapore, 2008)
44. J. Stejskal, Polyaniline: Preparation of a conducting polymer. Pure Appl. Chem. **74**, 857–867 (2002)
45. S. Zeghina, J.-L. Wojkiewicz, S. Lamouri, B. Belaabed, N. Redon, Enhanced microwave absorbing properties of lightweight films based on polyaniline/aliphatic polyurethane composites in X band. J. Appl. Polym. Sci. **131**, 40961 (2014)
46. M. Saha, S. Mukherjee, P. Bera, Md.M. Seikh, A. Gayen, Structural, optical, dielectric, and magnetic properties of spinel MFe_2O_4 (M = Co and Zn) nanoparticles synthesized by CTAB-assisted hydrothermal method. Ceram. Int. **48**, 35719–35732 (2022)
47. S.H. Hosseini, S.H. Mohseni, A. Asadnia, H. Kerdari, Synthesis and microwave absorbing properties of polyaniline/$MnFe_2O_4$ nanocomposite. J. Alloys Compd. **509**, 4682–4687 (2011)
48. J. Du, T. Li, Z. Xu, J. Tang, Q. Qi, F. Meng, Structure–activity relationship in microstructure design for electromagnetic wave absorption applications. Small Struct. **4**, 2300152 (2023)
49. P. Saini, V. Choudhary, B.P. Singh, R.B. Mathur, S.K. Dhawan, Polyaniline–MWCNT nanocomposites for microwave absorption and EMI shielding. Mater. Chem. Phys. **113**, 919–926 (2009)
50. T.K. Gupta, B.P. Singh, S.R. Dhakate, V.N. Singh, R.B. Mathur, Improved nanoindentation and microwave shielding properties of modified MWCNT reinforced polyurethane composites. J. Mater. Chem. A **1**, 9138–9149 (2013)
51. G. Yin, Y. Wang, W. Wang, D. Yu, Multilayer structured PANI/MXene/CF fabric for electromagnetic interference shielding constructed by layer-by-layer strategy. Colloids Surf. A **601**, 125047 (2020)

52. G. Yin, Y. Wang, W. Wang, Z. Qu, D. Yu, A flexible electromagnetic interference shielding fabric prepared by construction of PANI/MXene conductive network via layer-by-layer assembly. Adv. Mater. Interfaces **8**, 2001893 (2021)
53. M.N. Taj, B.D. Prasad, R. Narapareddy, H. Nagabhushana, G. Ramakrishna, B. Mahesh, S.T. Dadami, PANI-molybdate nanocomposites: Structural, morphological and dielectric properties for the effective electromagnetic interference (EMI) shielding application in X-band. Appl. Surf. Sci. Adv. **7**, 100203 (2022)
54. S. Khasim, Polyaniline-graphene nanoplatelet composite films with improved conductivity for high performance X-band microwave shielding applications. Results Phys. **12**, 1073–1081 (2019)
55. M.M. Ismail, S.N. Rafeeq, J.M.A. Sulaiman, A. Mandal, Electromagnetic interference shielding and microwave absorption properties of cobalt ferrite $CoFe_2O_4$/polyaniline composite. Appl. Phys. A **124**, 380 (2018)
56. K. Qian, Q. Zhou, H. Wu, J. Fang, M. Miao, Y. Yang, S. Cao, L. Shi, X. Feng, Carbonized cellulose microsphere@void@MXene composite films with egg-box structure for electromagnetic interference shielding. Compos. Part A **141**, 106229 (2021)
57. B. Zhao, C. Zhao, M. Hamidinejad, C. Wang, R. Li, S. Wang, K. Yasamin, C.B. Park, Incorporating a microcellular structure into PVDF/graphene–nanoplatelet composites to tune their electrical conductivity and electromagnetic interference shielding properties. J. Mater. Chem. C **6**, 10292–10300 (2018)

Publisher's Note